Nanoscale

PAPER

View Article Online
View Journal | View Issue

Cite this: *Nanoscale*, 2021, **13**, 5045

Optimizing plasmon enhanced luminescence in silicon nanocrystals by gold nanorods†

Ondřej Pavelka, *[a] Sergey Dyakov,[b] Jozef Veselý, [c] Anna Fučíková, [a] Hiroshi Sugimoto, [d] Minoru Fujii [d] and Jan Valenta *[a]

Received 5th January 2021,
Accepted 22nd February 2021

DOI: 10.1039/d1nr00058f

rsc.li/nanoscale

The great application potential of photoluminescent silicon nanocrystals, especially in biomedicine, is significantly reduced due to their limited radiative rate. One of the possible ways to overcome this limitation is enhancing the luminescence by localized plasmons of metallic nanostructures. We report an optimized fabrication of gold nanorod – silicon nanocrystal core–shell nanoparticles with the silica shell as a tunable spacer. The unprecedented structural quality and homogeneity of our hybrid nanoparticles allows for detailed analysis of their luminescence. A strong correlation between dark field scattering and luminescence spectra is shown on a single particle level, indicating a dominant role of the longitudinal plasmonic band in luminescence enhancement. The spacer thickness dependence of photoluminescence intensity enhancement is investigated using a combination of experimental measurements and numerical simulations. An optimal separation distance of 5 nm is found, yielding a 7.2x enhancement of the luminescence intensity. This result is mainly attributed to an increased quantum yield resulting from the Purcell enhanced radiative rate in the nanocrystals. The ease of fabrication, low cost, long-term stability and great emission properties of the hybrid nanoparticles make them a great candidate for bio-imaging or even targeted cancer treatment.

Introduction

Luminescent silicon nanocrystals (SiNCs) represent an important alternative to the conventional II–IV and III–V semiconductor quantum dots,[1] especially for biological applications. The natural abundance of silicon combined with low toxicity,[2] biocompatibility[3] and photostability[4] of SiNCs makes them a promising candidate for bio-imaging and related applications such as targeted cancer treatment.[5–8] A number of fabrication methods have been established for SiNCs in the past few decades, which ensure good control over the structural and optical properties of SiNCs.[9–12] The widely tunable emission band of SiNCs can span from visible (VIS) to near infrared (NIR) depending on the size and surface properties of the nanocrystals.[13] For biological imaging, mainly NIR emitting NCs are desirable as the tissue transparency window lies in this region. However, the indirect bandgap nature of silicon and relatively high number of surface traps limits the radiative rate of NIR emitting SiNCs.[14,15]

A commonly used strategy for emission enhancement of various photoluminescent quantum dots and organic dyes is a combination with metallic nanostructures (nanoparticles) supporting localized surface plasmon resonance (LSPR).[16] It is generally accepted that surface plasmons can influence the luminescence of nearby emitters in two ways – by increasing the absorption cross section of the fluorophores and by accelerating their emission rate due to increased local density of states (LDOS). The interaction depends on many parameters including size of the plasmonic particle, quantum yield of the fluorophore, distance between the two objects, spectral overlap of the particle's plasmonic resonance with absorption/emission band of the emitter, relative orientation of the emitter and particle dipole or even number of emitters coupled to a single particle.[16–18] The experimental observations range from significant enhancement[19,20] to strong quenching[21,22] of the luminescence depending on the particular situation. In many cases, however, a transition from enhancement to quenching with decreasing separation distance between the fluorophore and plasmonic particle has been theoretically predicted[17] and experimentally confirmed.[23,24]

[a]*Department of Chemical Physics and Optics, Faculty of Mathematics and Physics, Charles University, Ke Karlovu 3, 121 16 Prague, Czech Republic. E-mail: ondra.pavelka2@seznam.cz*
[b]*Photonics & Quantum Materials Center, Skolkovo Institute of Science and Technology, Nobel Street 3, Moscow 143025, Russia*
[c]*Department of Physics of Materials, Faculty of Mathematics and Physics, Charles University, Ke Karlovu 3, 121 16 Prague, Czech Republic*
[d]*Department of Electrical and Electronic Engineering, Graduate School of Engineering, Kobe University, Rokkodai, Nada, Kobe 657-8501, Japan*
†Electronic supplementary information (ESI) available. See DOI: 10.1039/d1nr00058f

In our study, gold nanorods (AuNRs) were chosen for plasmonic enhancement of luminescence in SiNCs for their stability, biocompatibility and ease of fabrication by means of colloidal chemistry.[25,26] Compared to spherical particles, nanorods exhibit higher scattering cross section and possess an additional widely tunable (longitudinal) plasmonic band which enables spectral overlap with the emission band of SiNCs. Plasmonic enhancement of SiNCs luminescence has been reported previously,[14,24,27,28] but none of the studies was able to achieve sufficiently high precision in the composite nanoparticle design while preserving low cost and application potential of the nanostructures. These reports show either theoretically[27] or experimentally[24] that an optimal separation distance between SiNCs and gold nanoparticles exists and is expected to be roughly 8–10 nm. However, due to difficultness of achieving the desired control in solution-based samples, a convincing evidence of the optimal distance for free standing particles is still lacking.

In this work, we aim at optimizing the fabrication process of colloidal AuNR-SiNC core–shell particles with controllable distance between the core nanorods and surrounding nanocrystals. We use amino-functionalized (APTS) silica (SiO_2) shell on AuNRs as an optically transparent tunable spacer to which the SiNCs are attached. The resultant colloidal solutions contain large quantity of nanoparticles with very well-defined design and can be produced at relatively low cost. The great precision of structural parameters enables us to perform optical measurements at single particle level which gives us an insight into the plasmon–luminescence coupling mechanism. Furthermore, the role of spacer thickness in emission rate enhancement is studied. Here, a combination of photoluminescence (PL) lifetime measurements and numerical (boundary element method; BEM) simulations was used yielding an optimum silica shell thickness of 5 nm. The origin of the PL intensity enhancement is discussed within the applied theoretical model and is mainly attributed to the quantum yield enhancement of SiNCs due to presence of AuNRs.

Experimental

AuNRs and SiNCs synthesis

AuNRs were prepared by applying small modifications to the well-established seeded growth method, first introduced by Nikoobakht and El-Sayed.[29] The protocol was customized to allow for control of aspect ratios of the NRs beyond what is possible by controlling silver concentration. Specifically, AuNRs 1 and AuNRs 2 were prepared by slow (5 h) addition (pumping) of the reducing agent (ascorbic acid) to the growth solution upon seeds addition and low aspect ratio of AuNRs 3 was achieved by cooling the growth solution to 20 °C in the first hour of NRs growth which causes significant changes to the reaction (reduction of Au+) kinetics. All procedures yield solutions of AuNRs capped by cetyltrimethylammonium bromide (CTAB). Dimensions of the NRs were measured from SEM images by analyzing minimum of 200 particles. Concentration of AuNRs in the solution was estimated using an empiric formula published by Edgar *et al.*[30] and by assuming the nanorod shape to be a cylinder with hemispherical caps. A standard synthesis yields an ~80 mL solution with 0.4 nM concentration of nanorods (6.8 mg of gold per batch).

SiNCs were prepared using a previously published protocol.[31] Briefly, cosputtering Si, SiO_2, B_2O_3 and P_2O_5 first yields Si rich borophosphosilicate glass which was then peeled off and annealed at 1100 °C in an N_2 gas atmosphere. SiNCs were then freed by etching in HF solution and dispersed in methanol. The average diameter of the NCs as measured from TEM images was ≈3.5 nm. A standard synthesis yields a ~1 mL solution with 33 nM concentration of nanocrystals (1.15 mg of silicon per batch).

SiO_2 coating, APTS functionalization and SiNCs attachment

Silica shells were grown on AuNRs using a single step protocol based on modified Stöber method.[32] For growth of thin shells, AuNRs were first centrifuged twice to remove excess CTAB and reduce its concentration to 1 mM and NaOH was added to adjust pH of the solution (final concentration of NaOH 1 mM). Finally, 2% tetraethyl orthosilicate (TEOS; v/v in methanol) was added so that the ratio between TEOS volume and total surface of AuNRs in the solution was $>0.4 \times 10^{-3}$ μl mm^{-2}. Magnetic stirring (300 rpm) and water bath (29 °C) were used for the reaction. Short centrifugation (4300*g*, 12 min) of the Au@SiO_2 NRs was used to stop the reaction, remove excess reactants and transfer the nanorods to ethanol or methanol.

Another 3 rounds of centrifugation were used before functionalization of the Au@SiO_2 NRs with APTS to reduce the residual water content in the alcohol solution. Concentration of the particles was adjusted to ≈0.2 nM. In a typical procedure, APTS (or APTS solution in ethanol or methanol) was then added so that ratio between APTS volume and total surface of Au@SiO_2 NRs was $\approx 0.1 \times 10^{-3}$ μl mm^{-2}. The reaction was allowed to proceed for 30 min under magnetic stirring (400 rpm) and elevated temperature (50 °C). Two centrifugation rounds were used for washing and the functionalized particles were redispersed in the original solvent (ethanol/methanol).

Finally, SiNCs were added to the nanorod solution in excess amount (total footprint of SiNCs ≥ total surface of Au@SiO_2 NRs) and the mixture was kept still for at least 24 h. Two more centrifugation rounds were used to remove unbound SiNCs while keeping the Au@SiO_2NRs@SiNCs in ethanol/methanol. In our typical experiment, the sufficient volume of Au@SiO_2NRs@AuNCs was relatively small (1 mL of 1 nM particles), but the protocol can be readily scaled up, if needed.

Characterization

Optical absorption spectra of the solutions were recorded with Specord 250 spectrophotometer (Analytik Jena). Zeta potentials of particles in the solution were measured with Zetasizer Nano ZS (Malvern Panalytical). Images of AuNRs and Au@SiO_2NRs were obtained from Auriga Compact SEM (Zeiss) operated at 7–15 kV. Images of SiNCs and Au@SiO_2NRs@SiNCs were recorded by JEOL JEM-2200FS, equipped with omega-filter,

and operated at 200 kV. For energy filtered images (EFTEM) a 2 eV wide slit at 16 eV was used to enhance the differences between crystalline Si and amorphous SiO_2 plasmon peak.[33] Solutions with particles were drop casted on a silicon wafer or lacey carbon coated copper grids (SPI) for SEM and TEM analysis, respectively.

Photoluminescence spectra and images were collected using a custom-built micro-spectroscopy setup based on an inverted optical microscope with spectrometer and liquid-nitrogen cooled CCD camera.[34] CW 405 nm laser was used for excitation. For measurement, small volume of the Au@SiO_2NRs@SiNCs solution was drop casted on a glass slide where fast evaporation of the solvent (alcohol) made the particles randomly distributed in a single layer. At sufficiently low nanorod concentrations this enabled us to perform measurements on a single particle level and avoid difficulties caused by emission reabsorption occurring in bulk liquid samples as discussed elsewhere.[16] The same setup was also used for dark field scattering measurements, where the particles were illuminated by an unpolarized white light source (halogen lamp) through a dark field condenser.

An analogous experimental setup was also used for lifetime measurements *via* time gated imaging. 50 μs pulses of a 405 nm laser were used for excitation. Time gate was usually set to 1 μs and 65 000 on CCD accumulations were collected for the given delay. At least 8 different spots on the substrate were studied for each sample with 20–100 emission sources on each spot. A summed signal from all the single sources was used for average lifetime fitting and calculation.

Electromagnetic simulations

For numerical simulations, PL was approximated by radiation of oscillating electric dipoles that are placed near AuNR. Purcell factor and excitation efficiency of dipoles in the vicinity of AuNRs were calculated by the boundary element method (BEM)[35] using the MNPBEM toolbox.[36,37] More details about the simulations and theoretical model for the calculations can be found in ESI.†

Results & discussion

Optimization of the fabrication process

Three types of gold nanorods that differ mainly by their aspect ratios were used in the experiments. By analyzing images from scanning electron microscope, we found the dimensions (length × width) of the nanorods as 66 × 20 nm (AuNRs 1), 69 × 23 nm (AuNRs 2) and 56 × 25 nm (AuNRs 3). The standard deviation of the dimensions is ≈10% for AuNRs 1 and AuNRs 3 and ≈15–20% for AuNRs 2 (the complete size distributions can be found in ESI, Fig. S1†). With aspect ratios ranging from 2.1 to 3.3, the longitudinal plasmonic bands of the nanorods appear in the red and near infrared spectral region. Absorption spectra of the nanorods are shown in Fig. 1, together with absorption and emission (PL) spectra of SiNCs. The broad emission of SiNCs in NIR overlaps with longitudinal

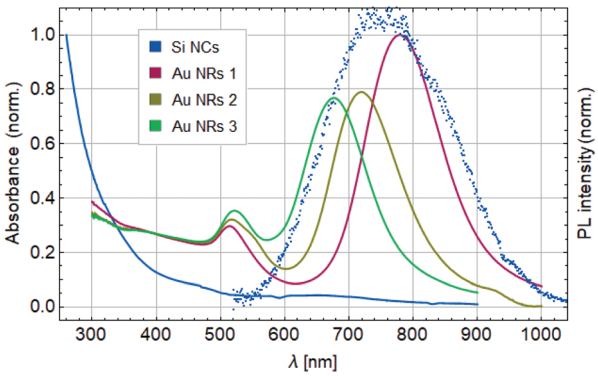

Fig. 1 Normalized absorption spectra of gold nanorod solutions (AuNRs 1, AuNRs 2, AuNRs 3) and solution of silicon nanocrystals (SiNCs). The dotted line represents luminescence spectrum of SiNCs.

plasmonic bands of all the three AuNR samples. As shown later in the paper, this overlap plays a very important role in coupling between luminescence of SiNCs and plasmons of AuNRs. Fig. 1 further shows that the absorption of SiNCs is strongest in UV and decreases rapidly at longer wavelengths. No major luminescence enhancement originating from increased absorption in SiNCs was therefore expected.

One of the major goals of this paper was to find an optimal distance between SiNCs and AuNRs which leads to the highest increase in radiative rate of SiNCs. It is well established that the distance between emitter and plasmonic structure represents a vital criterion in plasmon enhanced luminescence[38] and therefore fine control over this parameter was needed. The optimal separation distance of approximately 10 nm was expected based on previous theoretical predictions.[27] In our study, mesoporous silica (SiO_2) shells with variable thicknesses were grown on AuNRs to form a tunable spacer. Creation of the shells was based on a robust protocol which uses CTAB capped AuNRs as core structures and TEOS as a precursor for silica shells. Different parameters of the synthesis, such as TEOS and CTAB concentration, can allow for control over the resultant silica shell thickness and were used previously by other groups.[32,39,40] However, from our experience reducing the precursor concentration below certain limit leads to creation of nonuniform shells – probably due to a random nucleation of silica sites on AuNRs at low TEOS concentrations – and hence this approach makes growth of silica shells with good quality and thickness below 10 nm challenging. Therefore, in our synthesis we kept the TEOS concentration at sufficiently high level and controlled the shell thickness by reaction time instead. An increasing thickness of a silica layer on AuNRs effectively increases the local refractive index around the nanorods which results in gradual redshift of their longitudinal plasmonic peak. This enabled us to monitor the shell growth with conventional absorption spectroscopy and stop the reaction at the right moment by removing excess reactants by centrifugation. Moreover, this centrifugation step was used to remove excess CTAB from the nanorods and transfer the particles into non-aqueous solvent (mostly ethanol or methanol).

Fig. 2 summarizes synthesis of thin silica shells (5–15 nm) on AuNRs 1. As found from absorption spectra, the shell growth does not start before 45 min after addition of TEOS into the reaction solution. Then the increase in shell thickness was almost linear for approximately 3 h (60 min–150 min), which is when the desired shells can be obtained. In the rest of the solution the reaction was allowed to proceed for another 45 h, during which a limit shell thickness was reached. SEM images in Fig. 2 confirm good uniformity of the shells even for low thickness around 5 nm. With increasing thickness, the shells usually tend to be thicker at the sides of the rods than at the tips (labeled as dW and dL respectively in Fig. 2c), however the difference is <1 nm for such thin shells. Therefore, these SiO_2 coated AuNRs (Au@SiO_2 NRs) represent a solid starting point for distance dependent plasmon enhanced luminescence studies of SiNCs.

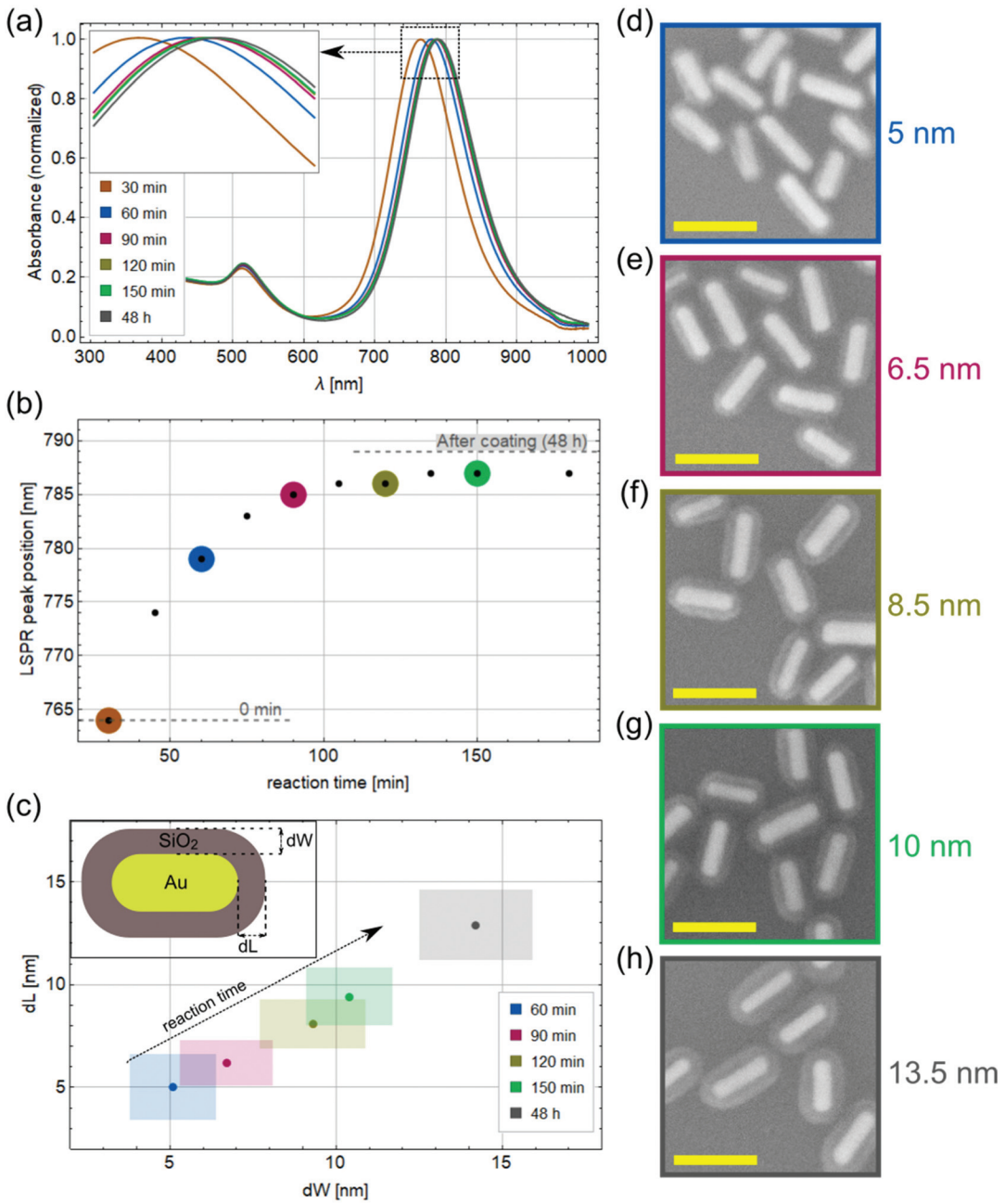

Fig. 2 Growth of silica shells on AuNRs monitored by absorption spectroscopy and SEM imaging. (a) Absorption spectra of AuNRs recorded at different times after coating onset. (b) Positions of the longitudinal LSPR peaks extracted from (a). The original (0 min) and final (48 h) peak positions are indicated by dashed lines. (c) Increase in silica shell thicknesses along the two main axes of AuNRs as measured from SEM images. The rectangles represent standard deviations of the mean values. (d)–(h) SEM images of Au@SiO_2NRs with increasing shell thicknesses (scale bar is 100 nm in all images). The color code is fixed in all graphs/images and links data obtained by stopping the reaction at given times between 30 min and 48 h.

In our work all-inorganic SiNCs were used which are co-doped by boron and phosphorus but do not have any protective ligands on their surface. High dispersibility of the SiNCs in polar liquids is ensured by special alignment of dopant atom pairs where the ionized boron atoms (B^-) are located closer to the surface of the NCs which induces their negative ζ-potential.[41] Since the ζ-potential of Au@SiO_2 NRs dispersed in alcohol is also negative, electrostatic repulsion would prevent SiNCs from attaching to the NRs. Au@SiO_2 NRs were therefore further functionalized with aminosilanes (APTES or APTMS; common abbreviation APTS) upon which the ζ-potential of the particles changed to positive values.

Silanization of SiO_2 surface with APTS is a key step of the whole fabrication process. The reaction must be well under control in order to preserve low thickness and high uniformity of the shells, but at the same time the APTS layer must provide sufficient colloidal stability to the particles. In order to optimize the functionalization protocol, we investigated the influence of several parameters on silanization of Au@SiO_2 NRs, such as water content, particle and APTS concentration, solvent or temperature. We used a combination of absorption spectroscopy and ζ-potential measurements to monitor the process and evaluate its result.

Fig. 3 highlights the difference between "successful" and "failed" functionalization. As shown in the insets of Fig. 3c and d, in both cases the ζ-potential of the particles is sufficiently high for long term colloidal stability (>40 mV). Yet, as shown in the TEM images, bad functionalization conditions can lead to uncontrolled condensation of APTS in the solution, which corrupts uniformity of the silica shells and causes aggregation of the particles. This is confirmed by absorption spectra recorded before and after the functionalization as any broadening of the longitudinal plasmonic peak of the nanorods indicates their aggregation. Successful functionalization is thus evidenced by negligible changes in the absorption spectra and high ζ-potential, even after removing excess APTS by centrifugation.

Detailed discussion of different aspects of silica silanization are beyond the scope of this paper, but still we would like to point out some of our experimental observations. The most important parameter by far is water content in the reaction solution. Although some water is needed in the solution

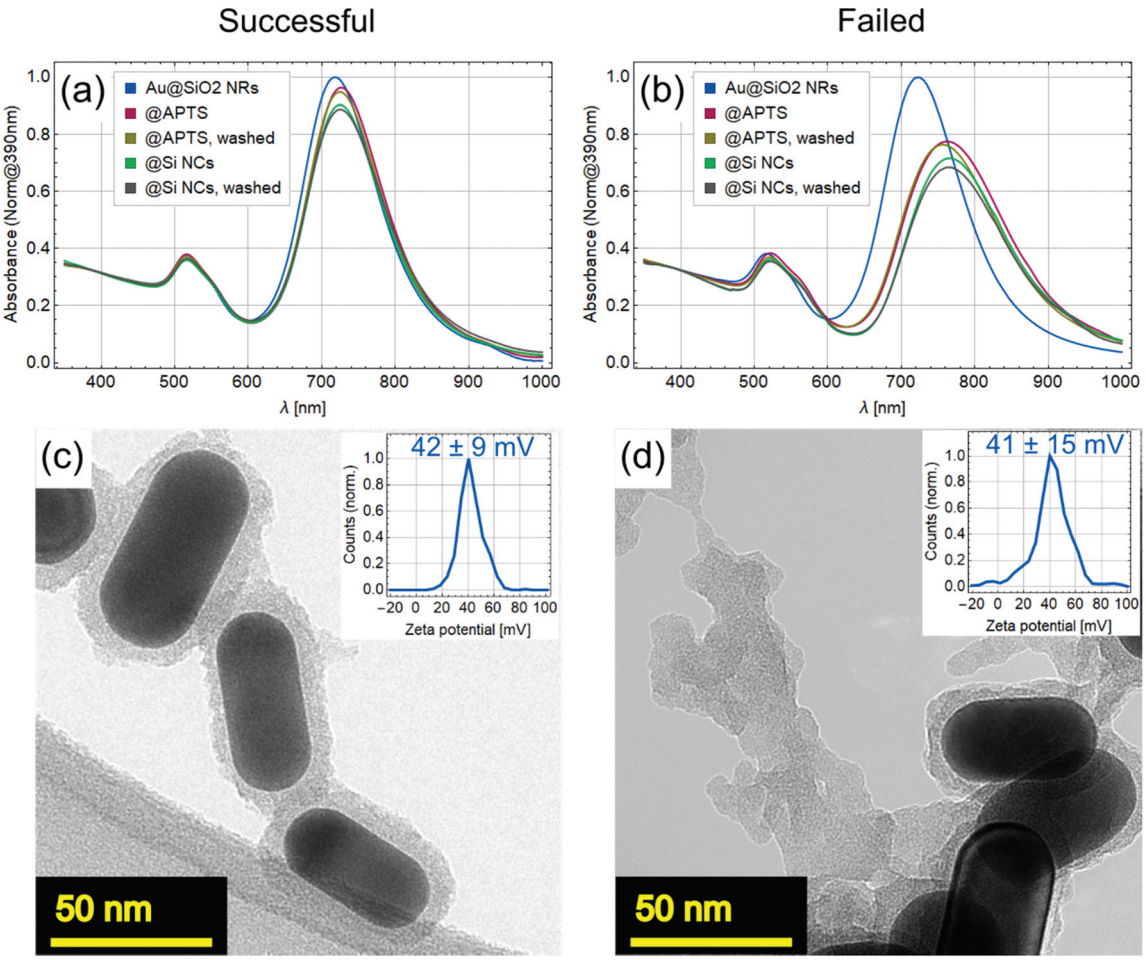

Fig. 3 APTS functionalization of Au@SiO_2 NRs monitored with absorption spectroscopy and TEM imaging. The difference between successful (a) and (c) and failed (b) and (d) functionalization is evidenced by longitudinal LSPR peak broadening and occurrence of uncontrolled local condensation of APTS around Au@SiO_2 NRs.

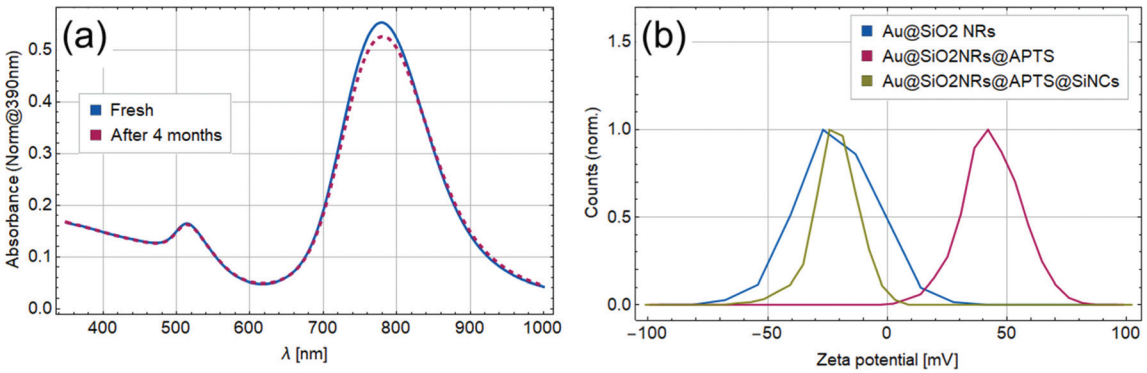

Fig. 4 Long term colloidal stability of Au@SiO_2NRs@SiNCs solution evidenced by (a) no changes in absorption spectra even after 4 months of shelf life and (b) high absolute value of zeta potential caused by rich loading of SiNCs on Au@SiO_2 NRs.

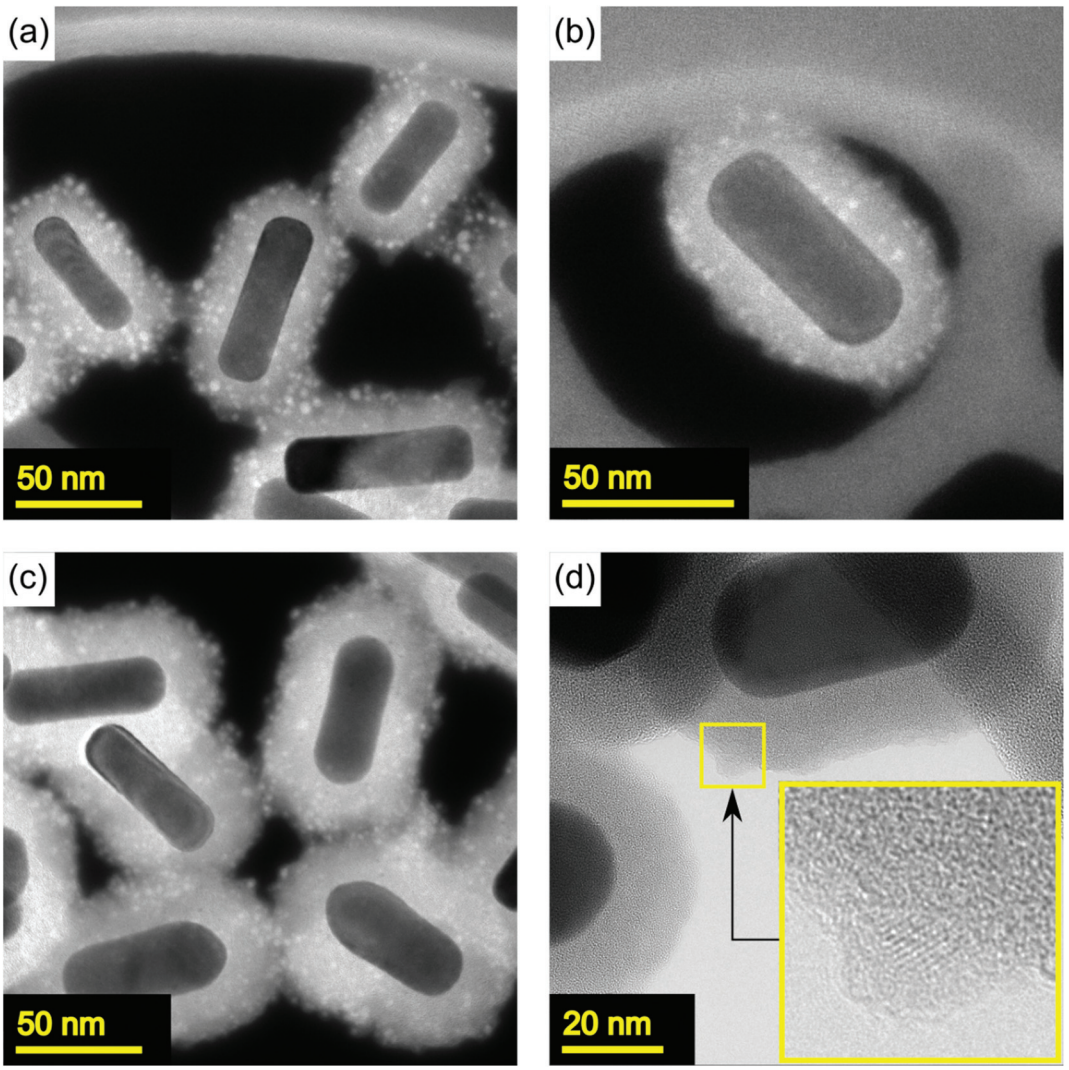

Fig. 5 (EF)TEM images of Au@SiO_2NRs@SiNCs. (a) and (b) 12 nm SiO_2 shell on AuNRs 1, (c) 20 nm SiO_2 shell on AuNRs 2, (d) 13 nm SiO_2 shell on AuNRs 2. Inset of (d) shows a single SiNC with visible lattice fringes.

to allow for hydrolysis of APTS, its content should be kept low to avoid uncontrolled reaction. For this reason, at least 4 centrifugation rounds need to be used for washing the Au@SiO_2 NRs before silanization, which is when the particles are transferred from water to alcohol. For the other parameters, less particle aggregation can be achieved by reducing particle concentration (<0.1 nM), shortening reaction time (<1 h), using APTMS rather than APTES and slightly elevating the reaction temperature (50 °C). No clear trend was observed for running the reaction in different solvents – using both ethanol and methanol yielded good results. Importantly, the functionalization did not cause any significant increase in the thickness of the silica shells (<0.5 nm based on analysis of TEM images of particle before and after functionalization respectively).

After the APTS functionalization, Au@SiO_2 NRs were coated with SiNCs simply by mixing the two solutions and allowing the QDs to electrostatically bind to the NRs (yielding Au@SiO_2NRs@SiNCs). Two additional centrifugation (washing) rounds were used to get rid of unbound SiNCs. Here again, recording absorption spectra of the solutions helped us confirm that no major changes in Au@SiO_2 NRs stability were caused by attaching SiNCs to their surface (see Fig. 3a and b). Moreover, the colloidal stability of the final solutions is preserved even in long term, as evidenced in Fig. 4a which compares absorption spectra of freshly prepared Au@SiO_2NRs@SiNCs with the same solution after 4 months of aging. Basically no difference in the spectrum shape was found which indicates excellent stability of the sample. This is further confirmed also by measuring the ζ-potential as shown in Fig. 4b. The ζ-potential starts at negative values for Au@SiO_2NRs, then changes to positive values after APTS functionalization but shifts back to negative values when SiNCs are attached to their surface. The mean ζ-potential value of −23 mV ensures sufficient long-term (several months) stability of the final sample and also points at rich loading of the QDs on Au@SiO_2 NRs.

High quality of the Au@SiO_2NRs@SiNCs samples was finally confirmed also by TEM measurements. Energy filtered TEM technique (EFTEM) was used to enhance the contrast between SiNCs and silica, which made evaluation of the SiNCs attachment significantly better. In addition, lacey carbon TEM grids were used because they enable background-free imaging of particles that end up resting in the holes of the film upon drop casting. EFTEM images shown in Fig. 5a–c clearly reveal superior quality of the samples. SiNCs are homogeneously attached to the surface of Au@SiO_2 NRs in relatively high concentrations while still preserving the shape uniformity of the shells.

For the shell thickness dependent studies, it is important to realize that what might seem as QDs placed at random distances from the golden nanorods is actually a 2D projection of a 3D object. Practically no free (unattached) SiNCs were observed on the TEM grids during the measurements which proves successful washing of the samples by centrifugation. This is very important for micro-spectroscopy studies as the measurements would be spoiled by free lying SiNCs. Fig. 5d shows a standard TEM image of SiNCs attached to Au@SiO_2NRs. At high magnification, lattice fringes of the SiNCs can be observed thus confirming their crystalline nature. However, such observation requires favorable orientation of the nanocrystal and therefore not all the NCs can be detected by this method. Moreover, with very poor contrast between silicon and silica it would be very difficult to evaluate the SiNCs attachment on a standard TEM image, which again highlights great relevance of employing the EFTEM technique. More EFTEM images are included in the ESI,† showing SiNCs attached to AuNRs 1 with different shell thicknesses (Fig. S2†) and a sample result of SiNCs attached to AuNRs 3 (Fig. S3†).

Photoluminescence measurements

A series of optical measurements was made to investigate the photoluminescence of SiNCs attached to Au@SiO_2 NRs. An example of PL image with Au@SiO_2NRs@SiNCs is shown in Fig. 6b where bright spots represent positions of the emitters.

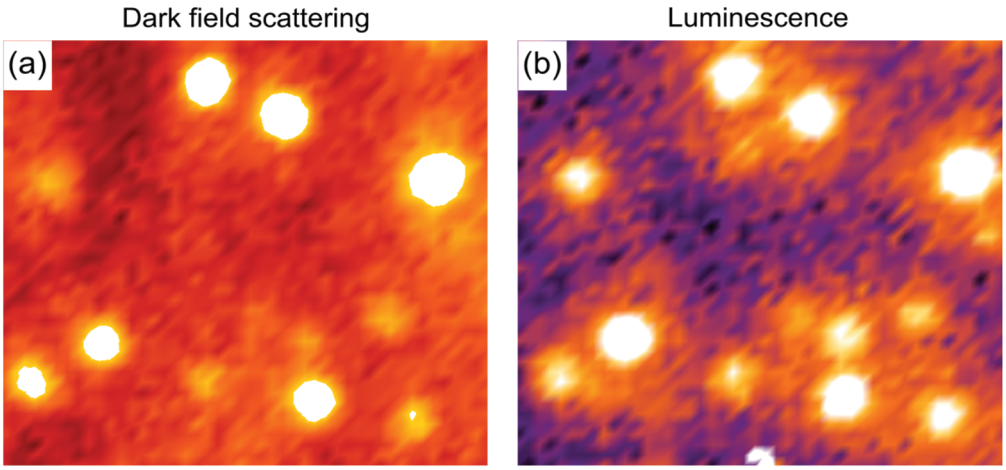

Fig. 6 (a) Dark field scattering and (b) photoluminescence images of Au@SiO_2NRs@SiNCs acquired from the same detection area. Color scales are only used to highlight intensity differences in the images and do not represent any spectral features of the measured objects.

Dark field image of the same region (Fig. 6a) confirms that SiNCs are only located where AuNRs are as each bright spot from luminescence is complemented by a bright spot in dark field. Different intensities of the spots are most likely caused by combination of effects including size distribution of AuNRs, variations in surface coverage of $Au@SiO_2$ NRs with SiNCs, and different orientations of the particles on the substrate causing variations in the intensity of signal collected in a polarization-dependent detection line of our setup.

To further investigate the emission properties of $Au@SiO_2$NRs@SiNCs we studied polarization of their luminescence. Using a quarter-wave plate we changed polarization of the excitation light from linear to circular and polarization analyzer was inserted into the detection line of the setup. Single particle spectra were recorded with different analyzer orientations from 0° to 180°, both in luminescence and dark field mode. An example of such measurement for SiNCs attached to AuNRs 1 with 10 nm shell is shown in Fig. 7. Extracting the peak intensity values from all the spectra in Fig. 7a and c yields polarization dependent datapoints which were fitted by $\sim\cos^2$ function (Fig. 7b and d). Result of this fit reveals that luminescence of SiNCs is coupled to longitudinal plasmon of the nanorods as evidenced by spectral position of the dark field scattering peak (at ~750 nm) and by the fact that the polarization dependence is identical for both types of measurement. Importantly the luminescence peak is centered at the very same wavelength as plasmon of the nanorod supporting our claim about plasmon–emission coupling.

In order to find out in which spectral range it is possible to achieve the plasmon–emission coupling, the same kind of measurement was also done for SiNCs attached to AuNRs 3 with plasmonic peak at lower wavelength (~670 nm). The result can be found in ESI (Fig. S4†) and shows an analogous polarization dependency match between luminescence and dark field scattering as in the previous case, just with the peaks centered at ~690 nm. Notably, the maximum intensity also occurs at different polarization than in Fig. 7 which excludes the option that the polarization would be caused by anisotropy of the detection line in our setup.

To get more insight into the origin of plasmon–luminescence coupling, we employed the above-described method to investigate the emission polarization for a large number of isolated $Au@SiO_2$NRs@SiNCs. Substrates with SiNCs attached to AuNRs 2 and AuNRs 3 were used. We looked at luminescence and dark field scattering peaks for each single measurement and studied how their spectral position relates to the polarization match. The result for sample with AuNRs 2 is shown in Fig. 8, where luminescence peak positions are plotted as a function of dark field scattering peak positions for cases when polarization match was observed (Fig. 8a) and was not observed (Fig. 8b). The insets in both graphs display histograms of peak luminescence wavelengths in the context of longitudinal plasmonic peak of AuNRs 2. A clear difference between the two cases was observed as the datapoints are nicely correlated when polarization matching occurred, while

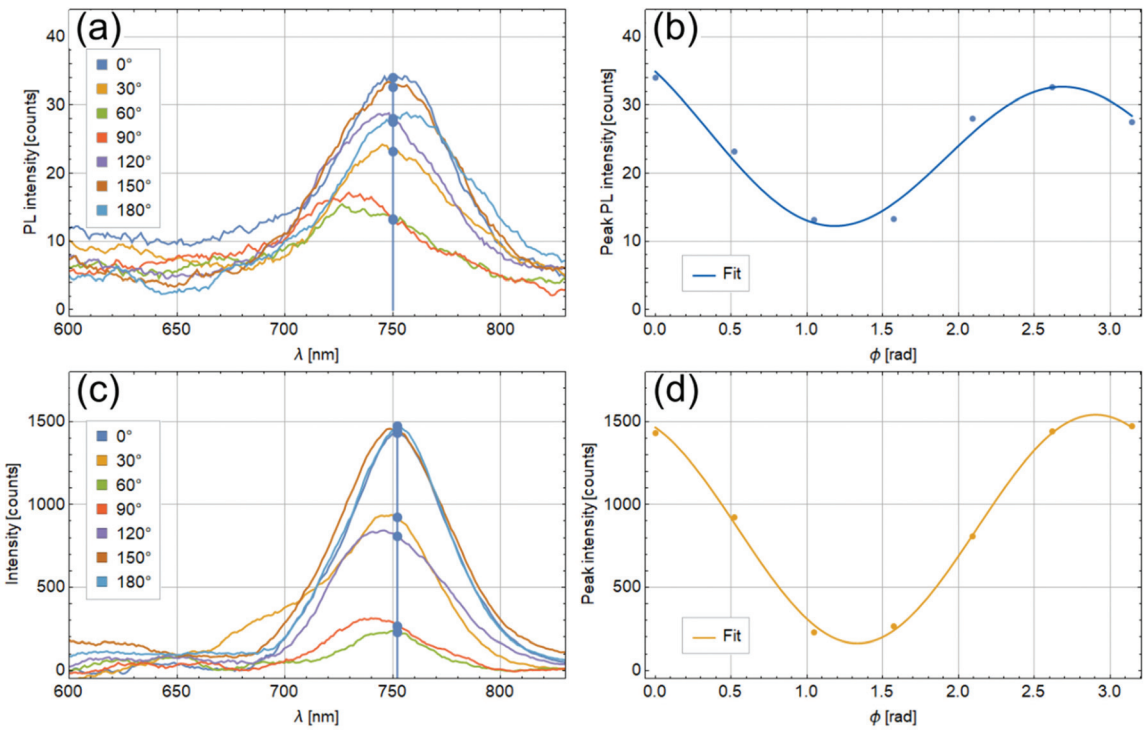

Fig. 7 Single particle measurement of (a) and (b) luminescence and (c) and (d) dark field scattering from $Au@SiO_2$NR@SiNCs for different polarizations. AuNRs 1 were used and the shell thickness was 10 nm. Peak values from (a) and (c) are plotted as a function of polarization in (b) and (d) respectively to visualize the same polarization dependency of PL and dark field scattering.

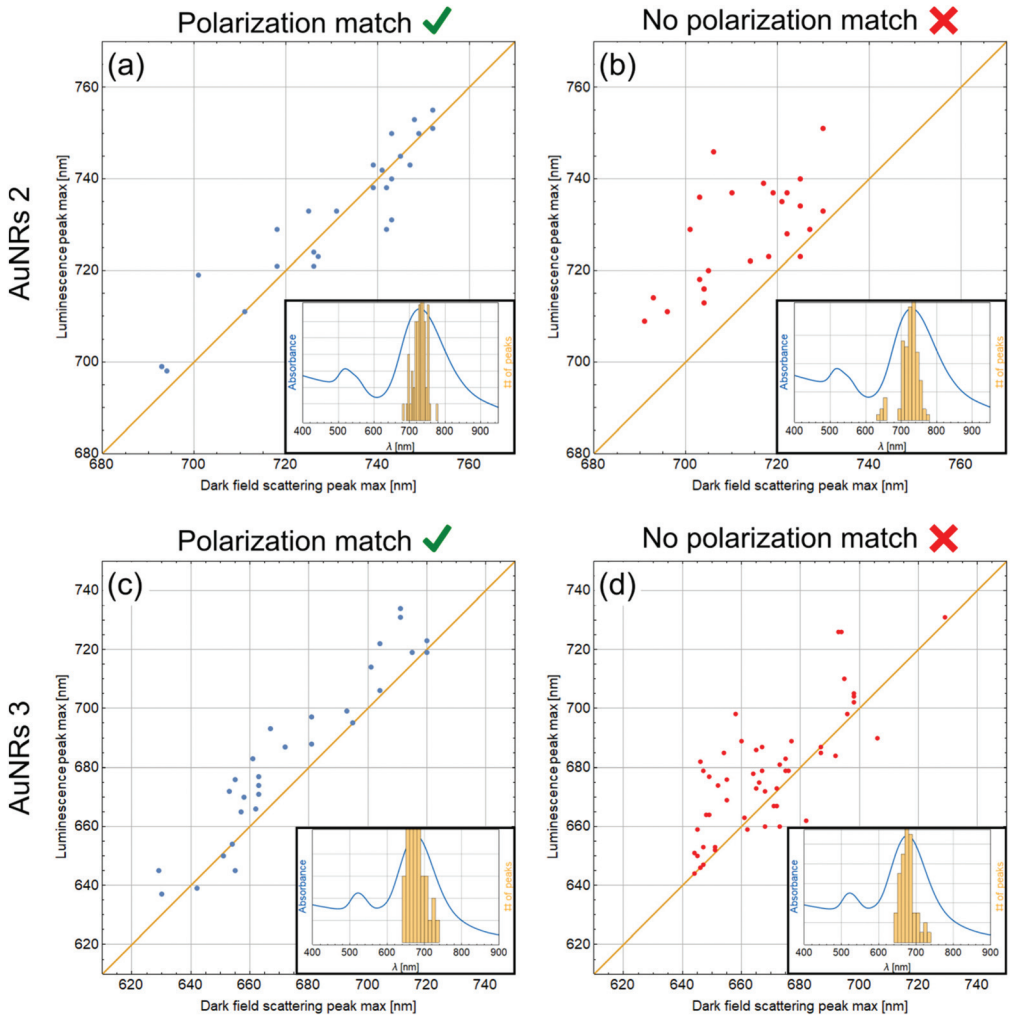

Fig. 8 Correlation between positions of luminescence and dark field scattering peaks measured for Au@SiO_2NRs@SiNCs prepared using (a) and (b) AuNRs 2 having LSPR at 750 nm and (c) and (d) AuNRs 3 having LSPR at 670 nm. (a) and (c) shows data from measurements where polarization match between PL and scattering was observed, (b) and (d) shows cases where it was not observed.

no apparent correlation was found for datapoints with no polarization matching. Interestingly, the luminescence peak distribution is the same in both cases and fits well with the ensemble plasmonic peak of AuNRs 2. This situation can be explained by suggesting that the plasmon–luminescence coupling can only occur when sufficient spectral overlap is achieved between LSPR of a particular nanorod and emission of the adjacent SiNCs. The unchanged PL peak distributions could be then just a coincidental result of good ensemble overlap between luminescence of SiNCs and plasmonic resonance of AuNRs. Although this explanation might sound plausible, how do we know that the coupling is a consequence of spectral match and not the other way round?

More information can be derived from measurements with AuNRs 3 having the plasmonic resonance band slightly offset from the SiNCs ensemble luminescence peak center. Following the same process as before, we arrived at results which are shown in Fig. 8c and d. Here again a good correlation between luminescence and scattering peaks can be observed in polarization matched cases (Fig. 8c), although the luminescence is a little redshifted with respect to the plasmonic peaks in most cases. The more striking result is displayed in Fig. 8d. Even though no polarization matching was observed in these cases the luminescence peaks still appear very close to the plasmonic resonances of their respective nanorods. As a result, the luminescence peak distribution is again well fitted by the ensemble longitudinal plasmon peak of AuNRs 3 in both sets of measurements (see insets of Fig. 8c and d). This finding points at somewhat different overall picture of the plasmon–luminescence interplay. The plasmonic resonance of AuNRs seems to be so dominant that it can affect the emission of SiNCs across a broad spectral range (630–750 nm in our experiments). Note that there were no luminescence peaks found beyond 740 nm for SiNCs attached to AuNRs 3, even though the ensemble luminescence peak of the NCs is centered at ~750 nm. From a statistical point of view this is a very

unlikely situation should there be no influence from the nanorods in cases where no polarization matching was observed. Hence, a certain degree of plasmon–luminescence coupling was created in all cases. We should emphasize here that finding "no polarization match" was in majority of cases caused by observation of very weak on no polarization dependence at all, rather than observation of polarization dependence that does not match with dark field scattering. In other words, the luminescence intensity remained usually basically constant in the non-matched cases. The absence of polarization matching for some particles can be then explained first by competition between several emitters attached to a single nanorod whose contributions to the detected signal get averaged and second by too large spectral offset between luminescence of SiNCs and plasmon of AuNRs. This can lead an intermediate situation in which the plasmon–emission coupling is too weak to fully control the luminescence polarization but still affects the shape and position of its peak. Note that in non-matched cases the luminescence peak is almost always redshifted with respect to the corresponding plasmonic peak and interestingly the lower the central wavelength of plasmon, the bigger the redshift.

The polarization effect can be further smeared if the PL signal is collected from a group of randomly oriented nanorods instead of a single particle.

With the working plasmon–luminescence coupling, we could finally investigate the effect of different separation distances between SiNCs and AuNRs on the luminescence of the NCs. We did this by measuring luminescence lifetime for a set of Au@SiO_2NRs@SiNCs samples with different silica shell thicknesses. A time gated imaging method was used with pulsed 405 nm laser as an excitation source. Such experimental layout enabled us (again) to collect signal from isolated sources and then calculate the average lifetime value for the given sample. More details about the lifetime measurements and data processing can be found in ESI.†

We studied five samples prepared from Au@SiO_2NRs shown in Fig. 2, as their shell thicknesses were (based on theoretical predictions) in the region of most interest. The measured decay curves were fitted using 3-exponential function model:[42]

$$I(t) = c_1 \cdot e^{-t/\tau_1} + c_2 \cdot e^{-t/\tau_2} + c_3 \cdot e^{-t/\tau_3} \quad (1)$$

and the lifetimes were calculated as an amplitude average of the fit parameters:

$$\tau = \frac{\sum_i c_i \times \tau_i}{\sum_i c_i} \quad (2)$$

The fitted curves shown in Fig. 9a and b display the calculated lifetimes as a function of the silica shell thickness. As expected, the average lifetime decreases with decreasing shell thickness. For thicknesses below 10 nm the lifetime drops to ≈1 μs which is 10× shorter than what was found for the reference sample of pure SiNCs $\tau_{(ref)}$ = 11.3 ± 0.5 μs. This points at significant emission rate enhancement in SiNCs when coupled to AuNRs, which is attributable to an acceleration of the radiative decay due to Purcell effect. However, no direct conclusions about the PL intensity enhancement can be done based on this experiment, as the lifetime decrease can be partially caused by additional nonradiative decay pathways. This becomes especially true for ultrathin shells (≤5 nm) where luminescence quenching caused by energy transfer starts playing an important role.[43]

According to the nanosurface energy transfer (NSET) theory, an efficient nonradiative pathway opens for excited NCs near gold surface for a separation distance R_0, which can be calculated as:

$$R_0 = \frac{0.225 \cdot n^2 \cdot \eta_0 \cdot c^3}{\omega_D^2 \cdot \omega_F \cdot k_F} \quad (3)$$

where η_0 is the quantum yield of the donor (NCs), ω_F and k_F are the bulk gold angular frequency and Fermi vector, respectively, ω_D is the angular frequency of the donor (NC) electronic transition, c is the velocity of light in vacuum and n is the refractive index of the environment. For our system, the NSET separation distance is R_0 = 6.5 nm, which can explain the

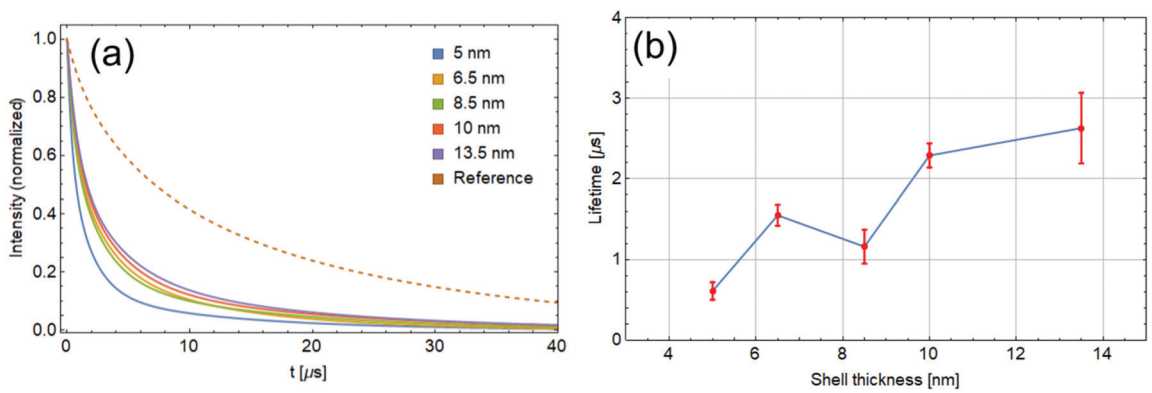

Fig. 9 (a) Fits of luminescence decays of SiNCs attached to Au@SiO_2 NRs with varying shell thicknesses. Decay of pure SiNCs is shown as a reference (dashed line). (b) Calculated average luminescence lifetimes of Au@SiO_2NRs@SiNCs as a function of SiO_2 shell thickness.

strong drop in lifetime for a 5 nm shell in Fig. 9b. This trend is expected to continue for even thinner shells, first due to the fast (d^{-4}) distance dependence of the resonant energy transfer[22] and second due to an additional nonradiative decay channel that can open in the form of charge transfer to the metallic particle.[16,44] Here the porosity of the silica shells has to be taken into account, as the size of the pores (≈4 nm)[32] is already comparable to the SiNC –AuNR distance. No more luminescence enhancement is therefore expected in this "ultrathin" shell region.

The number of NCs per NR is variable (unknown) in our samples. Therefore, no steady state PL measurements of the liquid samples can provide us with reliable information about the PL intensity enhancement, even if complications caused by reabsorption of the emitted photons in the bulk solution could be neglected. For this reason, we complement the experimental results with theoretical (boundary element method) simulations. In our model, PL is approximated by radiation of oscillating electric dipoles that are placed near Au@SiO_2 nanorod with variable silica shell thickness. Final results are obtained by averaging different dipole orientations and positions on the silica surface. More details about the model and derivation of the equations used in the following can be found in ESI.† Parameters of the simulation were chosen in a way that fits best the experimental situation and matches results of our measurements. As a first verification, an analogy of Fig. 2a and b is shown in ESI (Fig. S7†), that plots the calculated longitudinal LSPR peak positions as a function of silica shell thickness. An excellent match with the experiment is achieved, thus confirming validity of the structural and material parameters that were used. An appropriate choice of the optical properties of SiNCs (mainly radiative and nonradiative decay rates) were then verified by plotting the shell thickness dependence of the calculated PL lifetime and comparing it with our experimental values, as shown in Fig. 10c. With all the model parameters set, we used the simulations to estimate the PL intensity enhancement in our SiNCs–AuNR system.

According to the theory, the PL intensity ($I_{PL,0}$) of pure SiNCs is proportional to the excitation intensity ($I_{exc,0}$) and ratio between their radiative ($\Gamma_{rad,0}$) and total ($\Gamma_0 = \Gamma_{nr} + \Gamma_{rad,0}$) decay rate:

$$I_{PL,0} \propto I_{exc,0} \times \frac{\Gamma_{rad,0}}{\Gamma_{nr} + \Gamma_{rad,0}} \quad (4)$$

where Γ_{nr} is nonradiative decay rate. There are two ways of influencing the PL intensity by AuNRs – modifying the excitation intensity (I_{exc}) or the radiative rate of NCs. The latter is described by Purcell factor (f_{tot}) having external (f_{ext}) and absorbing (f_{abs}) parts which are responsible for far-field emission and electromagnetic losses, respectively. Please note that for the total, external, and absorbing parts of Purcell factor we use the notations like in the following references – [Ford *et al.*, 1984][45] and [Valenta *et al.*, 2019].[15] Then for the modified PL intensity we get:

$$I_{PL} \propto I_{exc} \times \frac{f_{ext}\Gamma_{rad,0}}{\Gamma_{nr} + f_{tot}\Gamma_{rad,0}} \quad (5)$$

The PL intensity enhancement ξ is then simply a ratio between the two quantities and takes the form of a product of

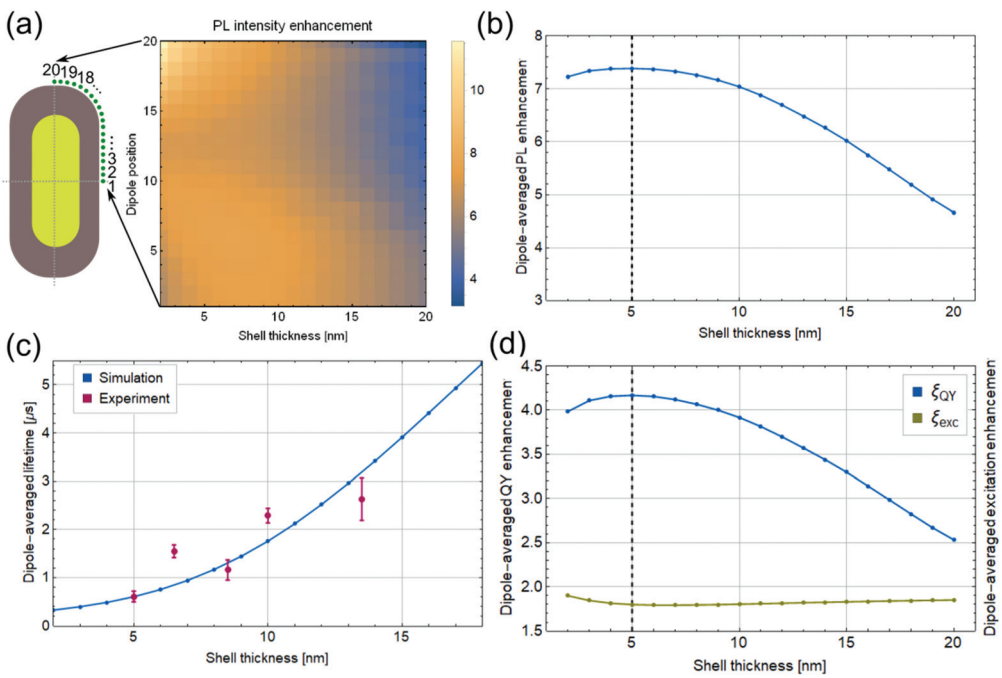

Fig. 10 PL intensity enhancement calculated from BEM simulations (a) for dipoles at varying positions and distances from the AuNR, (b) dipole position-averaged at varying distances from the AuNR. (c) Match between the theoretical and experimental PL lifetimes of samples with varying shell thickness. (d) Contributions of the excitation and QY enhancements to the overall PL intensity enhancement for varying shell thickness.

excitation enhancement (ξ_{exc}) and quantum yield enhancement (ξ_{QY}):

$$\xi = \frac{I_{PL}}{I_{PL,0}} = \frac{I_{exc}}{I_{exc,0}} \times \frac{f_{ext}(\Gamma_{nr} + \Gamma_{rad,0})}{\Gamma_{nr} + f_{tot}\Gamma_{rad,0}} = \xi_{exc} \times \xi_{QY}. \quad (6)$$

Fig. 10 summarizes the most important results of the calculations. In Fig. 10a PL intensity enhancement is shown as a function of silica shell thickness for individual NCs placed at different positions ranging from the middle of the NR side (position 1) to the very tip of the NR (position 20; see ESI† for the complete description). A dipole position-averaged enhancement (Fig. 10b) then exhibits an optimum shell thickness of 5 nm at which the PL intensity enhancement is the highest – ξ_{5nm} = 7.2. Fig. 10d shows the two main contributions to the PL intensity enhancement, *i.e.* excitation enhancement and quantum yield enhancement, where ξ_{QY} is clearly dominant and almost 2.5× bigger than ξ_{exc} for a 5 nm shell.

Our results are in a very good agreement with previous relevant studies. For example J. Goffard *et al.*[24] studied a very similar situation – SiNCs as fluorophore, silica used as a spacer, gold nanoparticles with LSPR tuned to emission wavelength of SiNCs in NIR. However, in contrast to our work a layered structure prepared by e-beam lithography was used here which allowed for sufficient control over the absolute number of SiNCs per gold nanoparticle and in the reference samples. Consequently, it was possible to obtain the optimum spacer thickness directly from the PL intensity measurements. The result of 8 nm silica thickness is very close to our result. In another two studies the optimum spacer thickness between gold and SiNCs was found to be 10 nm.[14,27] Note here that a perfect match between the individual results is unlikely as the absorption and scattering properties of different gold nanostructures depend on their morphology. Moreover, our numerical model does not account for any losses caused by energy or charge transfer from the excited NCs. Therefore, the 5 nm distance should be considered as the lower limit for optimum shell thickness. However, Fig. 10b shows that the peak in PL intensity enhancement is relatively flat and the enhancement factor remains high (>7) even for a 10 nm shell.

Conclusions

We report an optimized strategy for fabrication of core–shell AuNRs–SiNCs with silica shell as a tunable spacer. Fine control of various experimental parameters allowed us to prepare large quantities of the hybrid nanoparticles in colloidal solutions while preserving an excellent morphological homogeneity of the individual particles. The superior quality of our samples was confirmed by EFTEM images and a series of optical measurements. Plasmon–luminescence coupling was confirmed on a single particle level for a broad range of emission wavelengths using a combination of luminescence and dark field scattering measurements. Polarization studies further showed that the longitudinal plasmonic peak of AuNRs is dominant in determining the photoluminescence properties of the attached SiNCs. A combination of experimental and theoretical results was then used to calculate the PL intensity enhancement and its dependence on the silica spacer thickness. An optimum thickness of 5 nm was found yielding a 7.2× PL enhancement. The validity of our model is supported by an excellent match with the experimental measurements and by the obtained result, which is in a good agreement with other existing relevant studies. The low cost, high yield, and robustness of the fabrication process, together with excellent optical properties of our particles open a wide field of applications for Au@SiO_2NRs@AuNCs, especially in bio-imaging.

Conflicts of interest

There are no conflicts to declare.

Acknowledgements

This work was supported through the project of Charles University Research Center UNCE/SCI/010. A. F. was supported by Grant Agency of the Czech Republic, grant no 18-07977Y. H. S. and M. F. were supported by JSPS (Japan Society for Promotion of Science) KANENHI Grant No. 18K14092, 18KK0141, and 19K22111. We thank to Illia Fradkin for verifying the obtained values of Purcell factor with Comsol.

References

1 I. Sychugov, J. Valenta and J. Linnros, *Nanotechnology*, 2017, **28**, 072002.
2 K. Fujioka, M. Hiruoka, K. Sato, N. Manabe, R. Miyasaka, S. Hanada, A. Hoshino, R. D. Tilley, Y. Manome, K. Hirakuri and K. Yamamoto, *Nanotechnology*, 2008, **19**, 415102.
3 L. Ostrovska, A. Broz, A. Fucikova, T. Belinova, H. Sugimoto, T. Kanno, M. Fujii, J. Valenta and M. Hubalek Kalbacova, *RSC Adv.*, 2016, **6**, 63403–63413.
4 R. Mazzaro, F. Romano and P. Ceroni, *Phys. Chem. Chem. Phys.*, 2017, **19**, 26507–26526.
5 F. Erogbogbo, K.-T. Yong, I. Roy, R. Hu, W.-C. Law, W. Zhao, H. Ding, F. Wu, R. Kumar, M. T. Swihart and P. N. Prasad, *ACS Nano*, 2011, **5**, 413–423.
6 N. O'Farrell, A. Houlton and B. R. Horrocks, *Int. J. Nanomed.*, 2006, **1**, 451–472.
7 B. F. P. McVey and R. D. Tilley, *Acc. Chem. Res.*, 2014, **47**, 3045–3051.
8 A. Fucikova, J. Valenta, I. Pelant, M. Hubalek Kalbacova, A. Broz, B. Rezek, A. Kromka and Z. Bakaeva, *RSC Adv.*, 2014, **4**, 10334–10342.
9 O. Bisi, S. Ossicini and L. Pavesi, *Surf. Sci. Rep.*, 2000, **38**, 1–126.
10 L. Mangolini, E. Thimsen and U. Kortshagen, *Nano Lett.*, 2005, **5**, 655–659.

11 C. M. Hessel, E. J. Henderson and J. G. C. Veinot, *Chem. Mater.*, 2006, **18**, 6139–6146.
12 L. Pavesi and R. Turan, *Silicon Nanocrystals: Fundamentals, Synthesis and Applications*, John Wiley & Sons, 2010.
13 K. Dohnalová, A. N. Poddubny, A. A. Prokofiev, W. D. de Boer, C. P. Umesh, J. M. Paulusse, H. Zuilhof and T. Gregorkiewicz, *Light: Sci. Appl.*, 2013, **2**, e47–e47.
14 J. S. Biteen, D. Pacifici, N. S. Lewis and H. A. Atwater, *Nano Lett.*, 2005, **5**, 1768–1773.
15 J. Valenta, M. Greben, S. A. Dyakov, N. A. Gippius, D. Hiller, S. Gutsch and M. Zacharias, *Sci. Rep.*, 2019, **9**, 11214.
16 T. Ming, H. Chen, R. Jiang, Q. Li and J. Wang, *J. Phys. Chem. Lett.*, 2012, **3**, 191–202.
17 H. Mertens, A. F. Koenderink and A. Polman, *Phys. Rev. B: Condens. Matter Mater. Phys.*, 2007, **76**, 115123.
18 T. V. Shahbazyan, *Phys. Rev. B*, 2019, **99**, 125143.
19 S. Kühn, U. Håkanson, L. Rogobete and V. Sandoghdar, *Phys. Rev. Lett.*, 2006, **97**, 017402.
20 X. Ma, H. Tan, T. Kipp and A. Mews, *Nano Lett.*, 2010, **10**, 4166–4174.
21 P. Reineck, D. Gómez, S. H. Ng, M. Karg, T. Bell, P. Mulvaney and U. Bach, *ACS Nano*, 2013, **7**, 6636–6648.
22 T. Pons, I. L. Medintz, K. E. Sapsford, S. Higashiya, A. F. Grimes, D. S. English and H. Mattoussi, *Nano Lett.*, 2007, **7**, 3157–3164.
23 P. Anger, P. Bharadwaj and L. Novotny, *Phys. Rev. Lett.*, 2006, **96**, 113002.
24 J. Goffard, D. Gérard, P. Miska, A.-L. Baudrion, R. Deturche and J. Plain, *Sci. Rep.*, 2013, **3**, 2672.
25 N. J. Durr, T. Larson, D. K. Smith, B. A. Korgel, K. Sokolov and A. Ben-Yakar, *Nano Lett.*, 2007, **7**, 941–945.
26 A. Gole and C. J. Murphy, *Chem. Mater.*, 2004, **16**, 3633–3640.
27 H. Sugimoto, T. Chen, R. Wang, M. Fujii, B. M. Reinhard and L. Dal Negro, *ACS Photonics*, 2015, **2**, 1298–1305.
28 A. Inoue, M. Fujii, H. Sugimoto and K. Imakita, *J. Phys. Chem. C*, 2015, **119**, 25108–25113.
29 B. Nikoobakht and M. A. El-Sayed, *Chem. Mater.*, 2003, **15**, 1957–1962.
30 J. A. Edgar, A. M. McDonagh and M. B. Cortie, *ACS Nano*, 2012, **6**, 1116–1125.
31 M. Fujii, H. Sugimoto and K. Imakita, *Nanotechnology*, 2016, **27**, 262001.
32 I. Gorelikov and N. Matsuura, *Nano Lett.*, 2008, **8**, 369–373.
33 F. Iacona, C. Bongiorno, C. Spinella, S. Boninelli and F. Priolo, *J. Appl. Phys.*, 2004, **95**, 3723–3732.
34 J. Valenta and M. Greben, *AIP Adv.*, 2015, **5**, 047131.
35 F. J. García de Abajo and A. Howie, *Phys. Rev. B: Condens. Matter Mater. Phys.*, 2002, **65**, 115418.
36 U. Hohenester and A. Trügler, *Comput. Phys. Commun.*, 2012, **183**, 370–381.
37 J. Waxenegger, A. Trügler and U. Hohenester, *Comput. Phys. Commun.*, 2015, **193**, 138–150.
38 N. S. Abadeer, M. R. Brennan, W. L. Wilson and C. J. Murphy, *ACS Nano*, 2014, **8**, 8392–8406.
39 Q. Zhan, J. Qian, X. Li and S. He, *Nanotechnology*, 2009, **21**, 055704.
40 Z. Zhang, L. Wang, J. Wang, X. Jiang, X. Li, Z. Hu, Y. Ji, X. Wu and C. Chen, *Adv. Mater.*, 2012, **24**, 1418–1423.
41 H. Sugimoto, M. Fujii, K. Imakita, S. Hayashi and K. Akamatsu, *J. Phys. Chem. C*, 2012, **116**, 17969–17974.
42 M. Greben, P. Khoroshyy, I. Sychugov and J. Valenta, *Appl. Spectrosc. Rev.*, 2019, **54**, 758–801.
43 R. Prajapati, S. Chatterjee, A. Bhattacharya and T. K. Mukherjee, *J. Phys. Chem. C*, 2015, **119**, 13325–13334.
44 S. Dey and J. Zhao, *J. Phys. Chem. Lett.*, 2016, **7**, 2921–2929.
45 G. W. Ford and W. H. Weber, *Phys. Rep.*, 1984, **113**, 195–287.